(Received 13 December 2024, Accepted 21 December 2024, Scheduled 23 December 2024)

Dual-Modal Fluorescent Hyperspectral Micro-CT for Precise Bioimaging Detection

Jing Luo[1, 2, 3], He Zhu[1, 2, 3], Raheel Ahmed Janjua[1, 2], Wenbin Ji[2], Ruili Zhang[2], Junbo Liang[2], and Sailing He[2, 1, *]

[1] *Centre for Optical and Electromagnetic Research, National Engineering Research Center for Optical Instruments Zhejiang Provincial Key Laboratory for Sensing Technologies, College of Optical Science and Engineering Zhejiang University, Hangzhou 310058, China*

[2] *Zhejiang Engineering Research Center for Intelligent Medical Imaging, Sensing and Non-invasive Rapid Testing Taizhou Hospital, Zhejiang University, Taizhou, China*

[3] *These authors contributed equally*

ABSTRACT: In this study, we introduce a dual-modal fluorescence hyperspectral micro-CT system developed for, e.g., bioimaging applications. The system integrates an X-ray computed tomography (CT) module with a custom-designed hyperspectral fluorescence imaging module, achieving high-resolution structural imaging with detailed molecular-level insights. With a spectral resolution of 10 nm across the wavelength range of 450–750 nm, the hyperspectral fluorescence imaging module enables a fine compositional analysis. Using surface-modified nanoparticles, we demonstrate the system's capability to capture fluorescence under both X-ray and UV excitation. Imaging experiments on animal models further highlight the system's ability to generate comprehensive four-dimensional (4D) datasets that integrate spatial, spectral, and structural information. To the best of our knowledge, no such a dual-modal system or the like has even been reported before. This dual-modal approach enhances the visualization and analysis of biological tissues, offering promising applications in, e.g., disease diagnosis, surgical guidance, and preclinical research.

1. INTRODUCTION

Biomedical imaging techniques, such as computed tomography (CT) [1, 2], magnetic resonance imaging (MRI) [3, 4], and positron emission tomography (PET) [5, 6], are essential tools for diagnosing diseases, guiding treatments, and advancing biomedical research [7, 8]. These technologies have enabled the visualization of biological systems, providing powerful support for critical insights into their structure, function, and pathology. Among them, CT is particularly valued for its ability to produce high-resolution structural images [9]. Micro-computed tomography (micro-CT), a high-resolution 3D imaging technique similar to conventional CT, uses X-rays to penetrate samples from multiple angles, recording attenuation data to generate 2D projections [10, 11]. These projections are then reconstructed using computational algorithms to produce detailed 3D models of internal structures with micron-level spatial resolution and non-destructive imaging capabilities [12, 13]. Micro-CT has found extensive applications in studying bone microarchitecture [14–16], tumor imaging [15], pulmonary and soft tissue structures [17], and vascular networks [18]. Additionally, its high penetration and non-invasive nature have made it a valuable tool in biomaterials [19], geology [20], and industrial inspection [21]. However, micro-CT relies on X-ray attenuation for contrast, limiting its ability to capture molecular or functional information [22].

Hyperspectral imaging (HSI) captures detailed spectral information across tens to hundreds of spectral bands with nanometer-level bandwidths, providing molecular signal-related spectral data for each pixel in a spectral image [23–25]. This unique capability has made HSI a powerful tool for identifying and characterizing biological components such as tissues [26], cells [27], and biomolecules [28], which has been widely used in the field of biomedical diagnosis. However, its limited penetration depth restricts its application to deeper structures in biomedical imaging [29]. Combining HSI with micro-CT presents a promising approach to overcoming these limitations, though this field remains underexplored. The integration of HSI and micro-CT offers several advantages: it provides high-resolution 3D anatomical information combined with precise molecular spectral data, meeting the demand for multidimensional imaging in biomedical research. The high penetration depth of micro-CT complements the limitations of HSI, enabling comprehensive analysis of complex tissues. Furthermore, an integrated multimodal imaging system simplifies experimental workflows and enhances imaging efficiency.

Ju et al. developed a single-irradiation dual-modal imaging system based on micro-CT, combining the high penetration depth of micro-CT with the high sensitivity of optical imaging to achieve simultaneous CT and optical data acquisition [30]. Traditional optical imaging, however, struggles to analyze material composition, limiting its scope of application. Additionally, existing multimodal imaging systems face numerous chal-

* Corresponding author: Sailing He (sailing@zju.edu.cn).

FIGURE 1. (a) Schematic of our dual-modal fluorescence hyperspectral micro-CT system; (b) Physical photograph of the dual-modal system; (c) Internal rotating arm structure.

lenges, such as reliance on separate devices, which increases the complexity of image registration and data integration [31]. Real-time imaging and high-throughput capabilities are particularly critical in small animal studies. Balancing imaging resolution, molecular sensitivity, and multimodal information acquisition remains a significant technical challenge.

To address these challenges, we present a novel dual-modal hyperspectral fluorescence micro-CT system. By integrating hyperspectral imaging with micro-CT, this system enables simultaneous acquisition of structural and spectral molecular data. Unlike conventional approaches, it resolves alignment and integration issues while enhancing spectral, spatial, and temporal resolution. Validated in small animal models, the system demonstrates its capability to generate comprehensive 4D datasets, combining spatial, spectral, and structural insights. This innovation opens new avenues for biomedical imaging, offering significant potential in disease diagnosis, drug development, and surgical planning.

2. METHODS

2.1. System Setup

Figure 1 illustrates the dual-modal fluorescence hyperspectral micro-CT system, including the detailed optical path diagram in Figure 1(a), a physical representation in Figure 1(b), and internal rotating arm structure representation in Figure 1(c). As shown in Figure 1(a), the dual-modal fluorescence hyperspectral micro-CT primarily comprises three components: the X-ray CT imaging module (including the X-ray generator and X-ray detector), the conventional optical imaging module (CMOS1), and the hyperspectral imaging module. These three modules are aligned on the same plane to facilitate image registration and fusion between the CT and optical imaging systems. The X-ray generator and X-ray detector are positioned in a linear arrangement and mounted on a single rotating arm. Similarly, the conventional optical imaging module and hyperspectral imaging module are arranged in a straight line and mounted on another orthogonal rotating arm. This configuration effectively reduces radiation interference while clearly indicating the X-ray attenuation caused by the sample and capturing the luminescence generated by the nanostructured scintillator.

The hyperspectral imaging module, custom-developed for this system, is a key component designed to capture precise spectral data. It comprises four main elements: Lens 2, Lens 3, a tunable liquid crystal filter (LCTF) and CMOS2. The combination of Lens 2 and Lens 3 is used to eliminate chromatic aberration and form images on the CMOS sensor plane. Fluorescence emitted from the sample, excited by X-rays, passes through Lens 2 and Lens 3 before entering the LCTF. The LCTF, controlled electronically, sequentially transmits specific wavelengths within the 450–750 nm range. At each selected wavelength, the imaging lens directs the light onto a monochrome camera, which captures a series of wavelength-specific images. These images are then compiled to construct the full hyperspectral dataset. The spectral resolution of the system is determined by the transmission bandwidth of the LCTF, which is 10 nm, enabling the precise differentiation of spectral features in the captured data.

The sample is positioned at the system's center to ensure precise imaging. During operation, the two rotating arms enable a 360-degree rotation of the X-ray CT imaging module, the conventional optical imaging module, and the hyperspectral imaging module. The X-ray source emits a high-energy cone beam that penetrates the biological tissue and forms two-dimensional (2D) projection images on the flat-panel X-ray detector. Variations in X-ray attenuation caused by the distinct compositions of biological tissues result in differences across the detector images, capturing structural details at various layers. While the X-ray CT imaging module acquires 2D projection images from multiple angles, the hyperspectral imaging module simultaneously captures the fluorescence emitted by X-ray-excited nanoparticles. The conventional optical imaging module serves to adjust and align the sample's position with high precision. The acquired 2D X-ray projection images are reconstructed into a detailed three-dimensional (3D) CT model using advanced computational algorithms. To integrate the fluorescence data, hyperspectral images are aligned with the CT tomographic images through feature-based image registration. This fusion of structural and spectral information produces comprehensive dual-modal fluorescence hyperspectral CT images, offering both high-resolution anatomical details and molecular-level insights.

Notably, some nanoparticles and biological tissues can also emit fluorescence when excited by UV light at 405 nm. To capture more comprehensive data, an additional imaging step is performed after the hyperspectral CT imaging process. In this step, the X-ray source is turned off, and the sample is illuminated with UV light. The rotating arm operates in the same mode as during X-ray imaging, allowing the hyperspectral imaging module to collect spectral data corresponding to the UV-induced fluorescence. This UV-excited fluorescence data is then registered to the CT tomographic images using the same image alignment method. As a result, the final multimodal fluorescence CT model integrates fluorescence spectra from both X-ray and UV excitation along with detailed three-dimensional structural information. By combining these diverse features, the model provides a more comprehensive and precise dataset, significantly enhancing the depth and accuracy of biological imaging analyses.

2.2. Material Preparation

To evaluate the performance of our system, we synthesized and surface-modified phase-$NaGdF_4$ nanoparticles specifically for biological imaging analysis [32, 33]. The synthesized processes are described as follows: Europium-doped $NaGdF_4$ hexagonal phase nanoparticles were synthesized following the reported procedure1 after slight modification. 1 mmol of rare-earth (RE) oleates (Gd: Eu in a molar ratio of 0.95 : 0.05) were dissolved in 10 mL of ethanol in a three-neck glass flask, along with 5 mmol of sodium acetate. Subsequently, 10 mL of oleic acid and 10 mL of 1-octadecene were added, and the mixture was heated to 60°C to evaporate ethanol. The temperature was then increased to 160°C and maintained for 30 minutes under argon flow to remove residual gases, after which the solution was cooled to room temperature. A separate solution containing 4 mmol of NH_4F and 2.5 mmol of NaOH in 10 mL of methanol was then added to the flask. The mixture was heated at a rate of 20°C/min to 300°C, held at this temperature for 30 minutes, and allowed to cool naturally to room temperature. The product was precipitated with acetone, collected by centrifugation, and washed several times with ethanol. The final product was dispersed in hexane. The synthesis of core-shell nanoparticles was conducted using a layer-by-layer approach. Initially, the shell precursor was prepared by combining a 2-mL aqueous solution of lanthanide acetates (1 M) with 10 mL of oleic acid and 10 mL of 1-octadecene in a 50-mL flask, followed by heating at 160°C for 40 min. After cooling to 50°C, preformed core nanoparticles dispersed in cyclohexane were introduced, along with 5 mL of a methanol solution containing NH_4F (4 mmol) and NaOH (2.5 mmol). The mixture was stirred at 50°C for 30 min, then heated to 290°C under argon for 1 h before cooling to room temperature. The nanoparticles were precipitated with ethanol, centrifuged at 6000 rpm for 5 min, washed with ethanol, and redispersed in hexane. Multi-shell nanoparticles were formed by repeating this procedure.

Initially capped with oleate ligands, the synthesized nanoparticles were subjected to surface modification using a standard ligand exchange. Briefly, a solution of poly (acrylic acid) (PAA, MW $\approx$ 1500) was prepared by dissolving 0.5 g of PAA in 15 mL of diethylene glycol and heating the mixture to 110°C under vigorous stirring and an argon atmosphere. A cyclohexane (10 mL) containing the nanoparticles (0.5 mmol) was injected into the preheated PAA solution. The resulting mixture was heated to 240°C and maintained at this temperature for 30 minutes under argon flow. Upon cooling to room temperature, 1 mL of a dilute hydrochloric acid solution (0.10 M) was added to precipitate the PAA-capped nanoparticles. The precipitates were isolated by centrifugation, washed multiple times with deionized (DI) water, neutralized with a dilute NaOH solution (0.01 M), and finally re-dispersed in phosphate-buffered saline (PBS, pH 7.4).

The resulting nanoparticles exhibited strong fluorescence under both X-ray and UV excitations, making them highly suitable for bioimaging applications. Their biocompatibility further supports their use in biological systems. Figures 2(a) and 2(c) presents the physical image and 3D CT image of the nanoparticle samples, respectively. Figures 2(b) and 2(d) illustrate their fluorescence spectra under UV and X-Ray excitation, respectively. It can be seen that the nanoparticle has two main fluorescent peaks located around 610 nm and 690 nm excited by both X-rays and UV 405 nm light, highlighting its dual-modal fluorescence capabilities.

3. RESULTS AND DISCUSSION

To demonstrate the bioimaging capabilities of the developed dual-modal fluorescence hyperspectral micro-CT system, we performed imaging experiments on a mouse model using the synthesized nanoparticles. The experimental workflow is outlined in Figure 3.

The experimental subjects were male BALB/c nude mice, 7–8 weeks old, of SPF grade, sourced from Jiangsu Qinglongshan Biotechnology Co., Ltd., China. The nude mouse was first placed in a chamber filled with anesthetic gas. Once fully anesthetized, the nanoparticles were injected subcutaneously into the abdominal region. The mouse was then carefully positioned at the center of the system's testing platform and connected to a gas anesthesia apparatus to maintain stability throughout the imaging process. The system captured tomographic CT images from multiple angles and simultaneously collected fluorescence hyperspectral data. These datasets were integrated using a feature-matching algorithm, resulting in a three-dimensional CT model enriched with fluorescence hyperspectral information. This dual-modal approach provides both structural and molecular insights, with the hyperspectral imaging offering detailed compositional information about the biological tissue. Such dual-modal data enhance the system's potential for accurate and comprehensive pathological analysis.

In the scintillator design, hexagonal-phase NaGdF4 was chosen as the host material due to its superior ability to attenuate and convert incident X-rays, primarily attributed to the advantageous properties of Gd^{3+} ions. With a high atomic number (64) and large X-ray attenuation coefficient, these ions efficiently absorb X-ray photons and act as sensitizers by transferring the energy to emissive lanthanide ions (Ln^{3+}). For visible emission under X-ray irradiation, Eu^{3+} ions were confined to the core of the nanocrystals as primary emitters due to their sharp

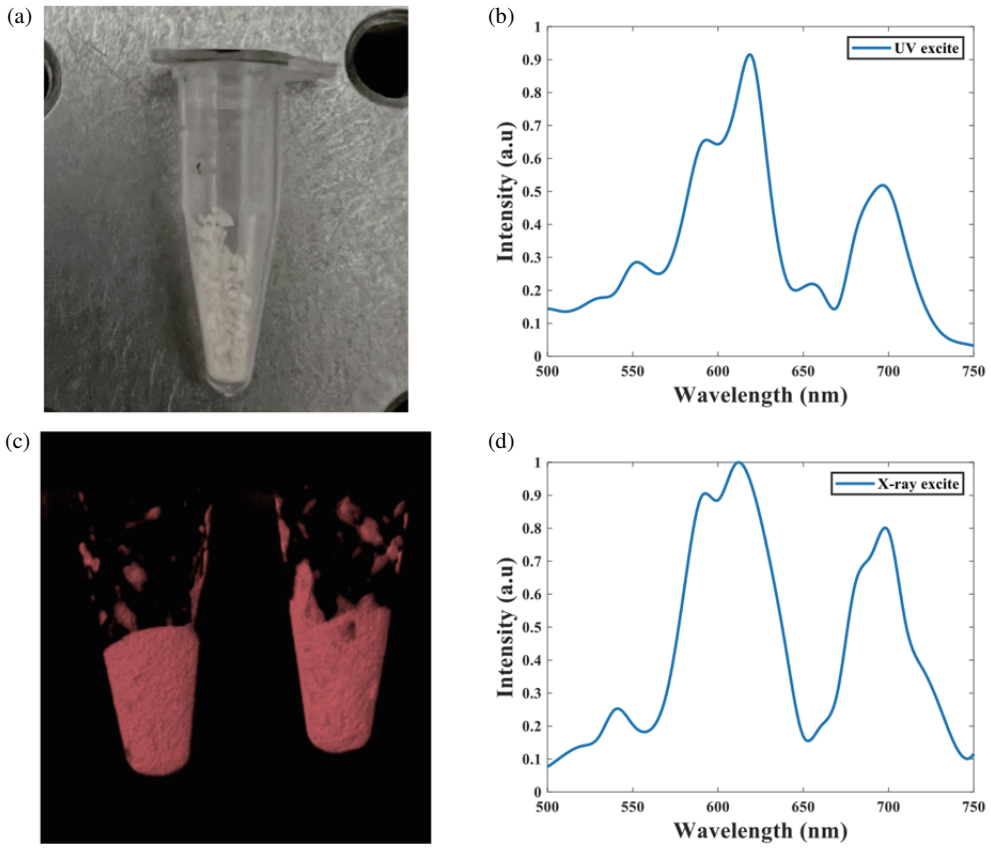

FIGURE 2. (a) Image of the nanoparticles; (b) Fluorescence spectrum under UV excitation; (c) Colored 3D CT image of the nanoparticles; (d) Fluorescence spectrum under X-Ray excitation.

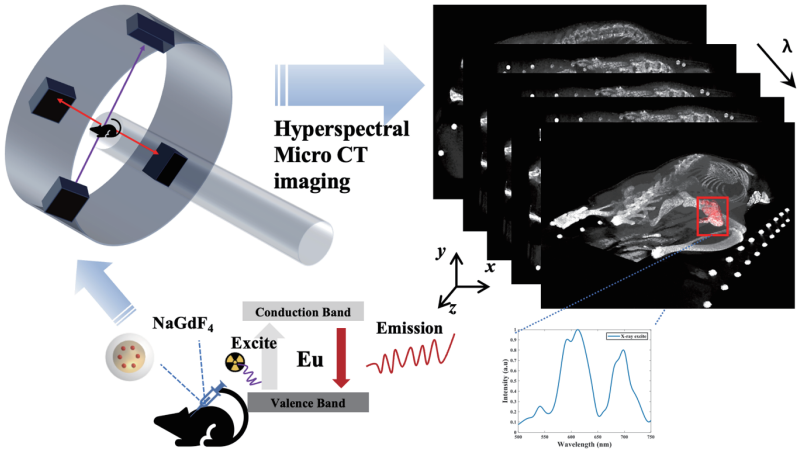

FIGURE 3. Workflow diagram of dual-modal fluorescence hyperspectral micro-CT imaging.

and characteristic f-f transitions. Ce^{3+} ions were incorporated into the inner shell to enhance energy absorption, where they effectively absorb X-rays and transfer the energy to surrounding Gd^{3+} ions. This energy is subsequently relayed to the Eu^{3+} ions in the core, resulting in efficient visible light emission. To address energy loss from surface defects, an optically inert NaGdF4 shell was introduced as the outermost layer. This shell significantly suppresses surface quenching effects (which usually will reduce the scintillation efficiency), and the high atomic mass of Lu enhances the X-ray mass attenuation coefficient, further improving the material's performance.

To determine the optimal X-ray and UV radiation intensities for achieving strong fluorescence signals, we analyzed the fluorescence spectra of the synthesized nanoparticles under varying radiation conditions, as shown in Figures 4(a) and 4(b). The results reveal that the fluorescence intensity is highest at an X-

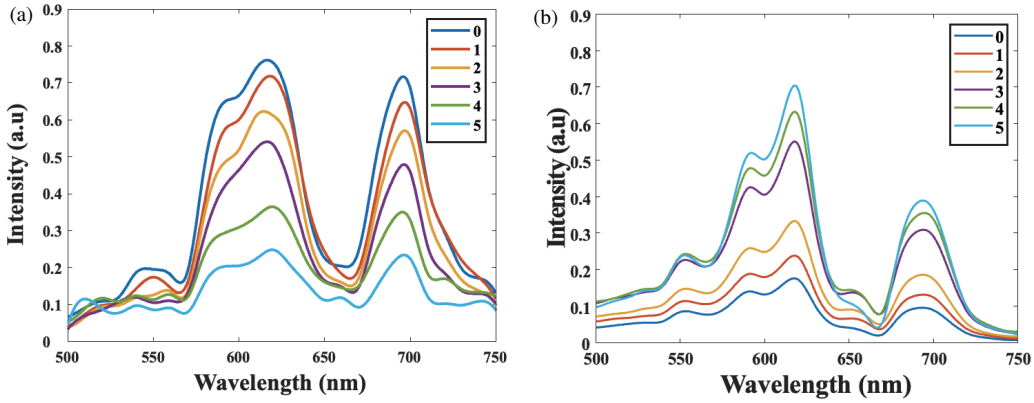

FIGURE 4. (a) Fluorescence spectra of nanoparticles under different X-ray intensities and (b) under different UV light intensities.

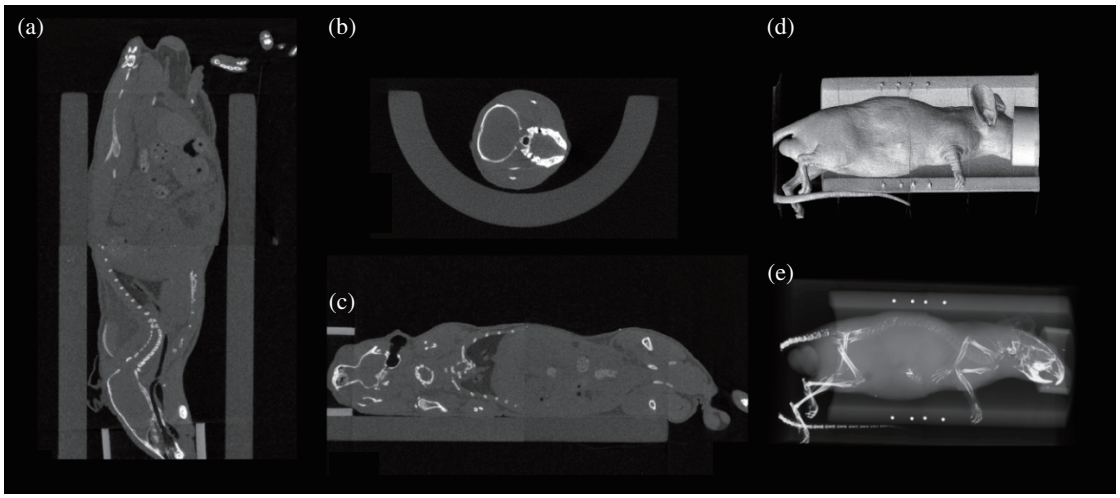

FIGURE 5. (a) Coronal, (b) transverse, and (c) sagittal tomographic CT images; (d) Three-dimensional surface CT model; (e) Three-dimensional bone CT model.

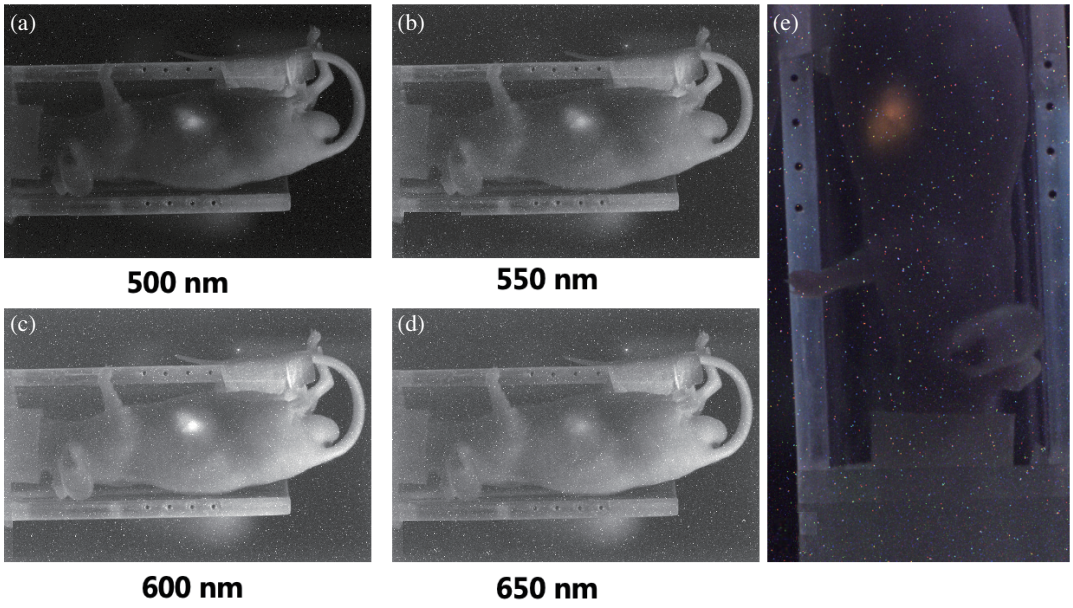

FIGURE 6. Fluorescence hyperspectral images at various wavelengths: (a)500 nm, (b) 550 nm, (c) 600 nm, and (d) 650 nm from a fixed viewing angle, with intensity determined by fluorescence signal strength. (e) False-color fluorescence hyperspectral image.

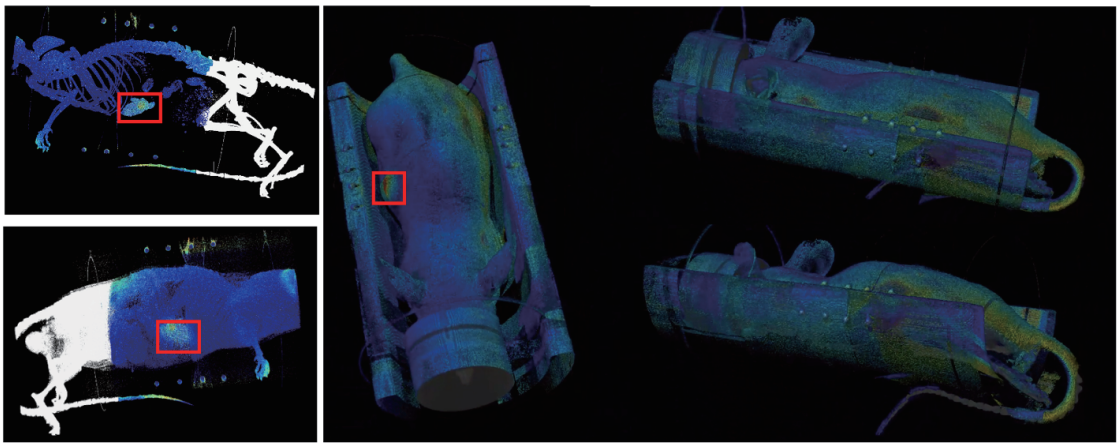

FIGURE 7. The dual-modal 4D CT image enhanced with fluorescence spectral data, with the nanomaterial locations marked by red boxes.

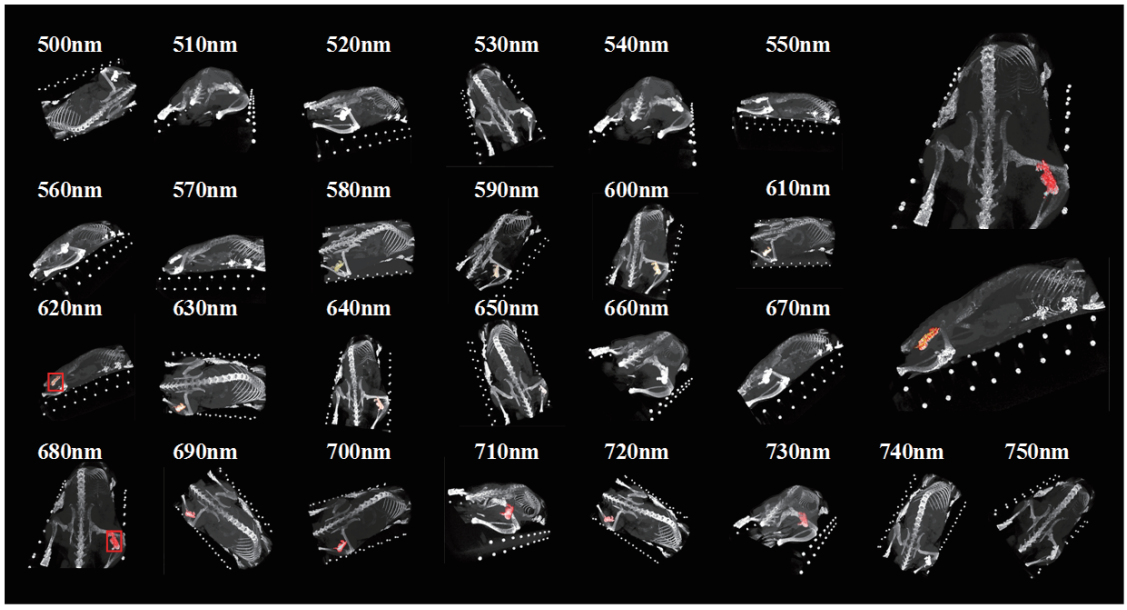

FIGURE 8. The 4D CT images of a nude mouse with nanoparticles injected intratumorally in the leg, displayed across different spectral bands.

ray voltage of 40 kV, corresponding label 0 in Figure 4(a). This occurs because higher-voltage X-rays penetrate deeper into the material, reducing absorption efficiency and, consequently, fluorescence activation. For UV radiation, the fluorescence intensity increases with UV power until it reaches a saturation threshold, beyond which no further enhancement is observed. Based on these observations, we selected an X-ray intensity of 40 kV for subsequent experiments, paired with a UV intensity below its saturation threshold. These settings ensure optimal fluorescence signal strength while minimizing unnecessary radiation exposure.

Figures 5(a)–(c) display the coronal, transverse, and sagittal tomographic CT images, respectively, while Figures 5(d) and 5(e) illustrate the reconstructed three-dimensional CT models. The variations in X-ray absorption between skin tissue and bone are evident, enabling clear differentiation based on their distinct CT attenuation values. Figures 6(a)–(d) present fluorescence hyperspectral images at various wavelengths from a fixed viewing angle, with intensity determined by fluorescence signal strength. A pronounced signal near 600 nm is clearly observed in Figure 6(c). Figure 6(e) shows a false-color fluorescence hyperspectral image, effectively revealing the spatial distribution and optical properties of the nanoparticles. This approach provides valuable complementary information to CT imaging, enhancing the overall imaging analysis.

Figure 7 illustrates the dual-modal 4D CT image enhanced with fluorescence spectral data, with the nanomaterial locations marked by red boxes. This model provides precise reconstruction of the subject, clearly delineating the spatial relationship between bone structures and nanoparticles, which holds promise for applications such as surgical guidance. Furthermore, the boundaries of nanomaterial aggregation are sharply defined.

Figure 8 presents the 4D CT images of another nude mouse with nanoparticles subcutaneously injected in the hind limb part, displayed across spectral bands ranging from 450 nm to 750 nm. The colors in the 4D CT model are assigned based on fluorescence intensity. In this model, only the regions where nanoparticles were injected exhibit fluorescence characteristics, with peak wavelengths around 610 nm and 690 nm. The two enlarged 4D CT images in Figure 8 show that at these two wavelengths, the nanoparticles in the hind limb display intense colors. Conversely, at other spectral bands, such as below 550 nm or above 740 nm, the fluorescence intensity is weak, and only the spatial distribution of the nanoparticles is visible in the 4D CT images. This is due to the partial absorption of X-rays by the nanoparticles. It is evident that conventional CT images can only reveal the spatial distribution of the nanoparticles but cannot distinguish them from other biological tissues or perform qualitative material analysis. In scenarios involving mixed materials injected in vivo or requiring further material characterization, traditional CT imaging shows certain limitations. The integration of hyperspectral imaging within the 4D CT framework captures the fluorescence properties of the nanoparticles, providing detailed insights into their characteristics and enabling analyses beyond the capabilities of conventional 3D CT imaging.

4. SUMMARY AND OUTLOOK

In this study, we have developed and validated a dual-modal fluorescence hyperspectral micro-CT system for precise bioimaging applications. The system integrates an X-ray CT module with a hyperspectral fluorescence imaging module, achieving high-resolution structural imaging and detailed spectral analysis. The custom-designed hyperspectral imaging module, based on a tunable filter structure, offers a spectral resolution of 10 nm across the 450–750 nm range. The system features an advanced design where the CT module and hyperspectral fluorescence imaging module are mounted on orthogonal rotating arms within a coplanar configuration. This arrangement effectively minimizes radiation interference, accurately reflects X-ray attenuation caused by the sample, and captures luminescence generated by nanoparticles. Through feature-matching algorithms, tomographic CT images are precisely registered and fused with hyperspectral fluorescence images, resulting in a multimodal CT model that integrates spatial, spectral, and structural information.

To validate the system's performance, imaging experiments have been conducted on animal models using custom-synthesized nanoparticles. These nanoparticles exhibit excellent biocompatibility and generate fluorescence signals around the 600 nm wavelength under X-ray or UV excitation. The system successfully demonstrated its capability to clearly depict bone and tissue structures, as well as the distribution and fluorescence properties of the nanoparticles in the test mouse. This highlights its potential applications in pathological analysis and surgical guidance. The molecular-level information provided by hyperspectral imaging complements traditional CT imaging, offering comprehensive support for the analysis of biological samples.

Future work will focus on enhancing the system's real-time imaging capabilities, optimizing data processing algorithms, and expanding its applicability to other imaging scenarios, such as tumor progression monitoring or therapeutic response evaluation. These advancements will further bridge the gap between research and clinical applications, laying a solid foundation for next-generation multimodal bioimaging technologies.

ACKNOWLEDGEMENT

This work is partially supported by the "Pioneer" and "Leading Goose" R&D Program of Zhejiang (No.2023C03083 and 2023C03135), the National Key Research and Development Program of China (Nos. 2022YFC3601000 and 2022YFC2010000), Ningbo Public Welfare Research Program Project (No. 2024Z234), the National Natural Science Foundation of China (No. W2412107), and Postdoctoral Fellowship Program of CPSF (GZC20232253). The authors are also grateful to Dr. Julian Evans of Zhejiang University for helpful discussion. The basic micro-CT system (Hiscan VM Pro Micro CT) was provided by Suzhou Hiscan Information Technology Co., Ltd.

REFERENCES

[1] Jaju, P. P. and S. P. Jaju, "Clinical utility of dental cone-beam computed tomography: Current perspectives," *Clinical, Cosmetic and Investigational Dentistry*, Vol. 6, 29–43, 2014.

[2] Cnudde, V. and M. N. Boone, "High-resolution X-ray computed tomography in geosciences: A review of the current technology and applications," *Earth-Science Reviews*, Vol. 123, 1–17, 2013.

[3] Schenck, J. F., "The role of magnetic susceptibility in magnetic resonance imaging: MRI magnetic compatibility of the first and second kinds," *Medical Physics*, Vol. 23, No. 6, 815–850, 1996.

[4] Edelman, R. R. and S. Warach, "Medical progress 1. Magnetic-resonance-imaging," *New England Journal of Medicine*, Vol. 328, No. 10, 708–716, 1993.

[5] Muehllehner, G. and J. S. Karp, "Positron emission tomography," *Physics in Medicine & Biology*, Vol. 51, No. 13, R117, 2006.

[6] Pahl, J. J., J. C. Mazziotta, G. Bartzokis, J. Cummings, L. Altschuler, J. Mintz, S. R. Marder, and M. E. Phelps, "Positron-emission tomography in tardive dyskinesia," *The Journal of Neuropsychiatry and Clinical Neurosciences*, Vol. 7, No. 4, 457–465, 1995.

[7] Han, X., K. Xu, O. Taratula, and K. Farsad, "Applications of nanoparticles in biomedical imaging," *Nanoscale*, Vol. 11, No. 3, 799–819, 2019.

[8] Judenhofer, M. S. and S. R. Cherry, "Applications for preclinical PET/MRI," in *Seminars in Nuclear Medicine*, Vol. 43, No. 1, 19–29, 2013.

[9] Webb, W. R., M. G. Stein, W. E. Finkbeiner, J. G. Im, D. Lynch, and G. Gamsu, "Normal and diseased isolated lungs: high-resolution CT," *Radiology*, Vol. 166, No. 1, 81–87, 1988.

[10] Maire, E. and P. J. Withers, "Quantitative X-ray tomography," *International Materials Reviews*, Vol. 59, No. 1, 1–43, 2014.

[11] Vásárhelyi, L., Z. Kónya, A. Kukovecz, and R. Vajtai, "Micro-computed tomography-based characterization of advanced materials: A review," *Materials Today Advances*, Vol. 8, 100084, 2020.

[12] Travincas, R., M. F. C. Pereira, I. Torres, A. Maurício, D. Silveira, and I. Flores-Colen, "X-ray microtomography applied to mortars: Review of microstructural visualization and parameterization," *Micron*, Vol. 164, 103375, 2023.

[13] Park, C. H., Z. R. Abramson, M. T. Jr., Q. Jin, J. Chang, J. M. Kreider, S. A. Goldstein, and W. V. Giannobile, "Three-dimensional micro-computed tomographic imaging of alveolar bone in experimental bone loss or repair," *Journal of Periodontology*, Vol. 78, No. 2, 273–281, 2007.

[14] Bouxsein, M. L., S. K. Boyd, B. A. Christiansen, R. E. Guldberg, K. J. Jepsen, and R. Müller, "Guidelines for assessment of bone microstructure in rodents using micro-computed tomography," *Journal of Bone and Mineral Research*, Vol. 25, No. 7, 1468–1486, 2010.

[15] Xu, Z., C. S. Locke, R. Morris, D. Jamison, K. M. Kozloff, and X. Wang, "Development of a semi-anthropomorphic photoacoustic calcaneus phantom based on nano computed tomography and stereolithography 3D printing," *Journal of Orthopaedic Research*, Vol. 42, No. 3, 647–660, 2024.

[16] Eberspächer-Schweda, M. C., K. Schmitt, S. Handschuh, A. Fuchs-Baumgartinger, and A. M. Reiter, "Diagnostic Yield of Micro-Computed tomography (micro-CT) versus histopathology of a canine oral fibrosarcoma," *Journal of Veterinary Dentistry*, Vol. 37, No. 1, 14–21, 2020.

[17] Yang, X., X.-J. Huang, Z. Chen, A.-L. Xu, H. Zhou, X.-L. Bi, P.-Y. Yan, and Y. Xie, "A novel quantification method of lung fibrosis based on Micro-CT images developed with the optimized pulmonary fibrosis mice model induced by bleomycin," *Heliyon*, Vol. 9, No. 3, e13598, 2023.

[18] Nebuloni, L., G. A. Kuhn, and R. Müller, "A comparative analysis of water-soluble and blood-pool contrast agents for in vivo vascular imaging with micro-CT," *Academic Radiology*, Vol. 20, No. 10, 1247–1255, 2013.

[19] Faraj, K. A., V. M. J. I. Cuijpers, R. G. Wismans, X. F. Walboomers, J. A. Jansen, T. H. v. Kuppevelt, and W. F. Daamen, "Micro-computed tomographical imaging of soft biological materials using contrast techniques," *Tissue Engineering Part C: Methods*, Vol. 15, No. 3, 493–499, 2009.

[20] Dierick, M., V. Cnudde, B. Masschaele, J. Vlassenbroeck, L. V. Hoorebeke, and P. Jacobs, "Micro-CT of fossils preserved in amber," *Nuclear Instruments and Methods in Physics Research Section A: Accelerators, Spectrometers, Detectors and Associated Equipment*, Vol. 580, No. 1, 641–643, 2007.

[21] Şık, A., H. Tanabi, H, E. Çubukçu, and B. Sabuncuoglu, "Experimental and analytical investigation of the tensile behavior of 3D-printed composites based on micro-CT analysis," *Journal of Thermoplastic Composite Materials*, Vol. 37, No. 7, 2356–2376, 2024.

[22] Clark, D. P. and C. T. Badea, "Advances in micro-CT imaging of small animals," *Physica Medica*, Vol. 88, 175–192, 2021.

[23] Luo, J., S. Li, E. Forsberg, and S. He, "4D surface shape measurement system with high spectral resolution and great depth accuracy," *Optics Express*, Vol. 29, No. 9, 13 048–13 070, 2021.

[24] Lu, G. and B. Fei, "Medical hyperspectral imaging: A review," *Journal of Biomedical Optics*, Vol. 19, No. 1, 010901, 2014.

[25] Xu, Z., E. Forsberg, Y. Guo, F. Cai, and S. He, "Light-sheet microscopy for surface topography measurements and quantitative analysis," *Sensors*, Vol. 20, No. 10, 2842, 2020.

[26] Yao, X., S. Li, and S. He, "Dual-mode hyperspectral bio-imager with a conjugated camera for quick object-selection and focusing," *Progress In Electromagnetics Research*, Vol. 168, 133–143, 2020.

[27] Zhu, S., K. Su, Y. Liu, H. Yin, Z. Li, F. Huang, Z. Chen, W. Chen, G. Zhang, and Y. Chen, "Identification of cancerous gastric cells based on common features extracted from hyperspectral microscopic images," *Biomedical Optics Express*, Vol. 6, No. 4, 1135–1145, 2015.

[28] Zhu, H., J. Luo, J. Liao, and S. He, "High-accuracy rapid identification and classification of mixed bacteria using hyperspectral transmission microscopic imaging and machine learning," *Progress In Electromagnetics Research*, Vol. 178, 49–62, 2023.

[29] Kim, E. B., Y. S. Baek, and O. Lee, "A study on the classification of atopic dermatitis by spectral features of hyperspectral imaging," *IEEE Access*, 2024.

[30] Ju, Q., S. Luo, C. Chen, Z. Fang, S. Gao, G. Chen, X. Chen, and N. Gu, "Single-irradiation simultaneous dual-modal bioimaging using nanostructure scintillators as single contrast agent," *Advanced Healthcare Materials*, Vol. 8, No. 9, 1801324, 2019.

[31] Xu, Z., W. Zhang, C. Quesada, X. Wang, and M. Fabiilli, "Longitudinal monitoring of angiogenesis in a murine window chamber model in vivo," *Tissue Engineering Part C: Methods*, Vol. 30, No. 3, 93–101, 2024.

[32] Janjua, R. A., C. Gao, R. Dai, Z. Sui, M. A. A. Raja, Z. Wang, X. Zhen, and Z. Zhang, "Na+-driven nucleation of NaYF4:Yb,Er nanocrystals and effect of temperature on their structural transformations and luminescent properties," *The Journal of Physical Chemistry C*, Vol. 122, No. 40, 23 242–23 250, 2018.

[33] Wang, F., R. Deng, and X. Liu, "Preparation of core-shell NaGdF4 nanoparticles doped with luminescent lanthanide ions to be used as upconversion-based probes," *Nature Protocols*, Vol. 9, No. 7, 1634–1644, 2014.